

# Aerosol Synthesis and Gas-Phase Photoelectron Spectroscopy of Ag-Bi-I Nanosystems

Danijela Danilović, Dušan K. Božanić,\* Radovan Dojčilović, Nenad Vukmirović, Pitambar Sapkota, Ivana Vukašinović, Vladimir Djoković, John Bozek, Christophe Nicolas, Sylwia Ptasinska, and Aleksandar R. Milosavljević\*

Cite This: *J. Phys. Chem. C* 2020, 124, 23930–23937

Read Online

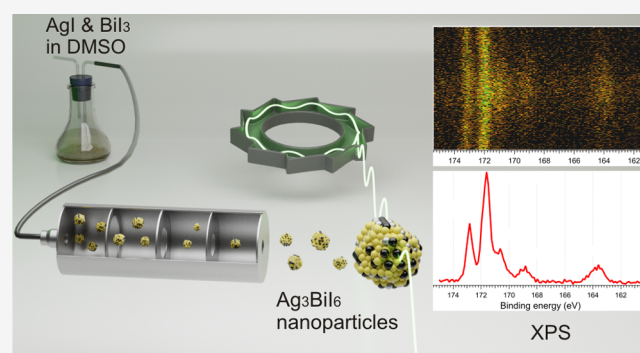
ACCESS |

Metrics & More

Article Recommendations

Supporting Information

**ABSTRACT:** We report on the aerosol generation of ligand-free silver iodobismuthate (Ag-Bi-I) nanoparticles (NPs) and on in situ investigation of their electronic structure using synchrotron radiation soft X-ray aerosol photoelectron spectroscopy (XAPS). The structural and morphological characterizations revealed the aerosol to be composed of spherical rudothite  $\text{Ag}_3\text{BiI}_6$  particles, approximately 100 nm in size. The XAPS showed well-resolved signals from all expected elements (Ag, Bi, and I) and allowed estimation of the NP work function to be about 4.5 eV. The ionization energy of  $\text{Ag}_3\text{BiI}_6$  NPs was determined to be 6.1 eV that is in good agreement with our calculations based on a hybrid functional approach. The presented method of production of  $\text{Ag}_3\text{BiI}_6$  aerosol can prove beneficial for the future development of Ag-Bi-I-based photovoltaic materials, since it allows the deposition of Ag-Bi-I particles on large surface areas of arbitrary shape and roughness.



## INTRODUCTION

Silver iodobismuthates (Ag-Bi-I) were recently proposed as a nontoxic replacement for lead halide perovskites as light-absorbing materials in photovoltaic applications.<sup>1–6</sup> Ag-Bi-I materials can be either produced in powder form using solid state preparation methods in a nonoxidative environment<sup>1</sup> or processed in the form of thin films.<sup>2–6</sup> Kim et al.<sup>6</sup> fabricated  $\text{AgBi}_2\text{I}_7$  thin films by spin-coating AgI and  $\text{BiI}_3$  powders dissolved in *n*-butylamine, whereas Khazee et al.<sup>2</sup> fabricated the same material using the coevaporation of AgI and  $\text{BiI}_3$ . The fabrication of Ag-Bi-I-based thin films facilitates their integration into photovoltaic devices and increases the power conversion efficiency (PCE) by reducing the distances traversed by the charge carriers. The photovoltaic solar cells fabricated using Ag-Bi-I thin films as absorber materials usually have PCEs around ~2% which are dependent on the Ag:Bi molar ratio.<sup>3</sup> Recently, Turkevych et al.<sup>4</sup> have presented a “rudothite” class of halides ( $\text{Ag}_a\text{Bi}_b\text{I}_x$ , where  $x = a + 3b$ ) and used them as an absorber material in solar cells. The prototype device containing a  $\text{Ag}_3\text{BiI}_6$  thin film showed a PCE at 4.3%.

Due to inherent transport characteristics of the nanoparticle (NP), the preparation of Ag-Bi-I nanometer-sized objects could enhance device performance and further facilitate the integration of Ag-Bi-I materials into the photovoltaic devices. However, to the best of our knowledge, there are no suitable procedures for Ag-Bi-I NP fabrication. In this study, we

therefore present a method for fabricating ligand-free Ag-Bi-I NPs in the form of aerosols. Since the highest PCE was reported for the  $\text{Ag}_3\text{BiI}_6$  rudothite, we focused on this material and examined its electronic properties. The electronic structure of  $\text{Ag}_3\text{BiI}_6$  NPs is investigated using synchrotron radiation (SR) soft X-ray aerosol photoelectron spectroscopy (XAPS).<sup>7,8</sup> This technique enabled us to study the electronic properties of isolated NPs in vacuum, avoiding any influence of the substrate. The effects of the particle charging and radiation damage<sup>9</sup> are negligible for nanoparticles in a beam that pass quickly through the ionizing radiation absorbing at most one photon. It should be emphasized that aerosols with ligand-free airborne NPs are suitable for further processing and deposition on large surface areas of arbitrary shape and roughness, which can lead to the low-cost and scalable aerosol processing<sup>10–12</sup> of Ag-Bi-I materials.

The rudothite  $\text{Ag}_3\text{BiI}_6$  NPs were prepared by atomizing a dimethyl sulfoxide (DMSO) solution of AgI and  $\text{BiI}_3$  powders. The formed aerosols were tested by XAPS immediately after

Received: July 25, 2020

Revised: September 18, 2020

Published: October 15, 2020



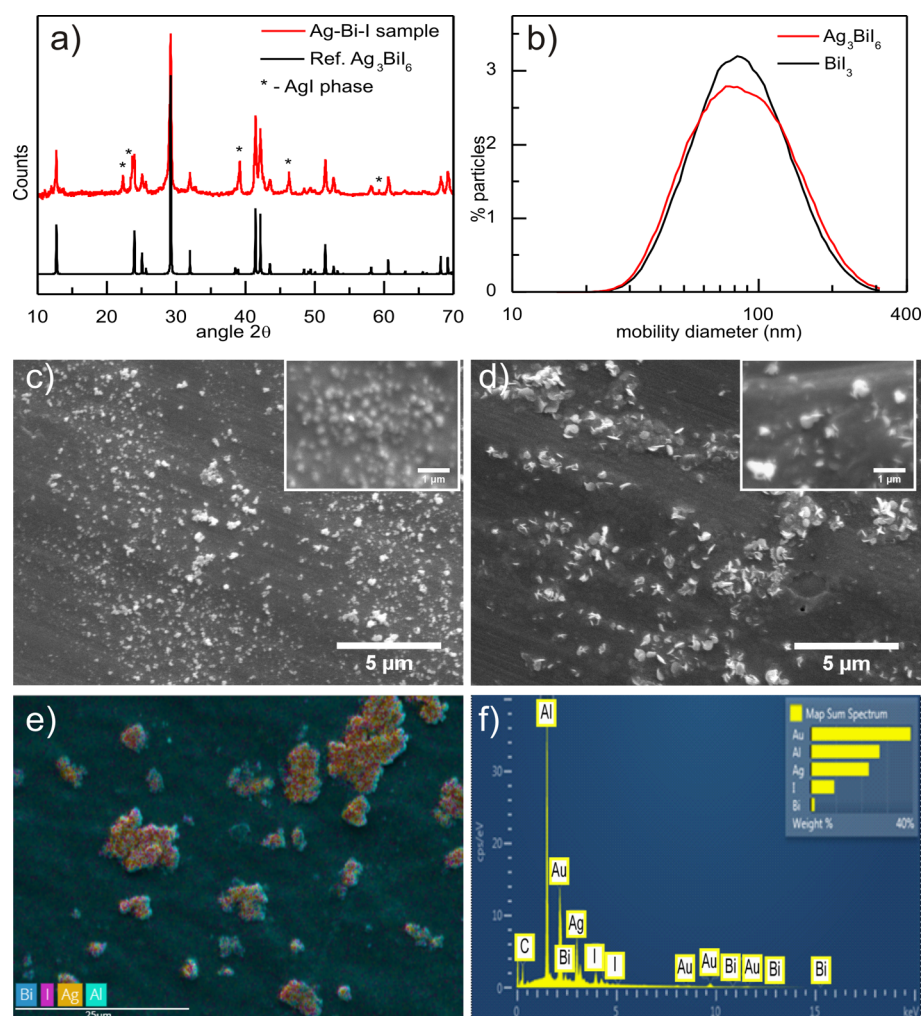


**Figure 1.** (a) XRD pattern of the Ag-Bi-I sample precipitated from DMSO (red line) and the reference  $\text{Ag}_3\text{BiI}_6$  pattern (black).<sup>4</sup> The asterisks denote peaks corresponding to the AgI phase. (b) Distribution of mobility diameters of the  $\text{Ag}_3\text{BiI}_6$  and  $\text{BiI}_3$  nanoparticles. Total particle concentration was in the order of  $10^6$  particles/ $\text{cm}^3$ . SEM images of (c)  $\text{Ag}_3\text{BiI}_6$  and (d)  $\text{BiI}_3$  particles on an aluminum substrate. Higher magnification SEM images of the samples are included as an inset. (e) Chemical microanalysis SEM image of a broad area of the Ag-Bi-I sample. (f) Energy dispersive X-ray spectra of the Ag-Bi-I sample (the presence of Al is from the substrate and Au from the sample coating layer).

preparation. The measurements were carried out with a tunable synchrotron radiation source, resulting in high resolution photoemission spectra in the investigated photoelectron kinetic energy range. The  $\text{BiI}_3$  aerosol was produced using the same atomization procedure and investigated by XAPS for comparison.

## EXPERIMENTAL AND THEORETICAL SECTION

Details of the fabrication procedure and experimental setup are provided in the Supporting Information (S.I.). Briefly, the transparent Ag-Bi-I solution (Figure S1) was first prepared via dispersion of the homogenized AgI/ $\text{BiI}_3$  powders in DMSO (molar ratio of Ag:Bi = 2:1, and total concentration of AgI +  $\text{BiI}_3$  was 1.058 wt/vol %). Since the solubility of AgI in DMSO is less than 0.01 mg/L, the optical transparency of the solution suggested coordination of  $\text{Ag}^+$  ions by the iodobismuthate anions.<sup>4</sup> Ag-Bi-I aerosols were generated by atomization of the precursor solution using TSI 3076 atomizer and the aerosol droplets were transported first through a metallic tube heated to 120 °C and then through a cold trap to remove excess DMSO (see Figure S2 and the Supporting Information for more details).

X-ray diffraction (XRD) measurements of the samples deposited on oriented Si wafer were performed by a Rigaku SmartLab system operating with  $\text{Cu K}\alpha$  radiation (1.5406 Å, 30 mA, 40 kV) in the  $2\theta$  range from 10 to 70°. The UV-vis absorption spectra of the samples were recorded on a Thermo Evolution 600 spectrophotometer.

Scanning electron microscopy (SEM) analysis of the samples precipitated on the Al substrate using a Nanometer Aerosol Sampler (TSI model 3089) was performed by a JEOL JSM-6390 LV instrument equipped with an energy dispersive X-ray analyzer at 15 kV operating voltage. For this characterization, the sample was additionally coated with a thin layer of gold.

XAPS was performed at the PLEIADES beamline at SOLEIL synchrotron, France, using the Multi-Purpose Source Chamber (MPSC).<sup>13</sup> More detailed description of the setup is provided in the Supporting Information and schematically shown in Figure S2. The XPS spectra were recorded using a  $\pm 30^\circ$  aperture wide-angle lens VG-Scienta R4000 electron energy analyzer, at incident photon energies of 100, 380, 720, and 800 eV, depending on a desired ionization energy (valence or inner shell). The photon beam was produced by a

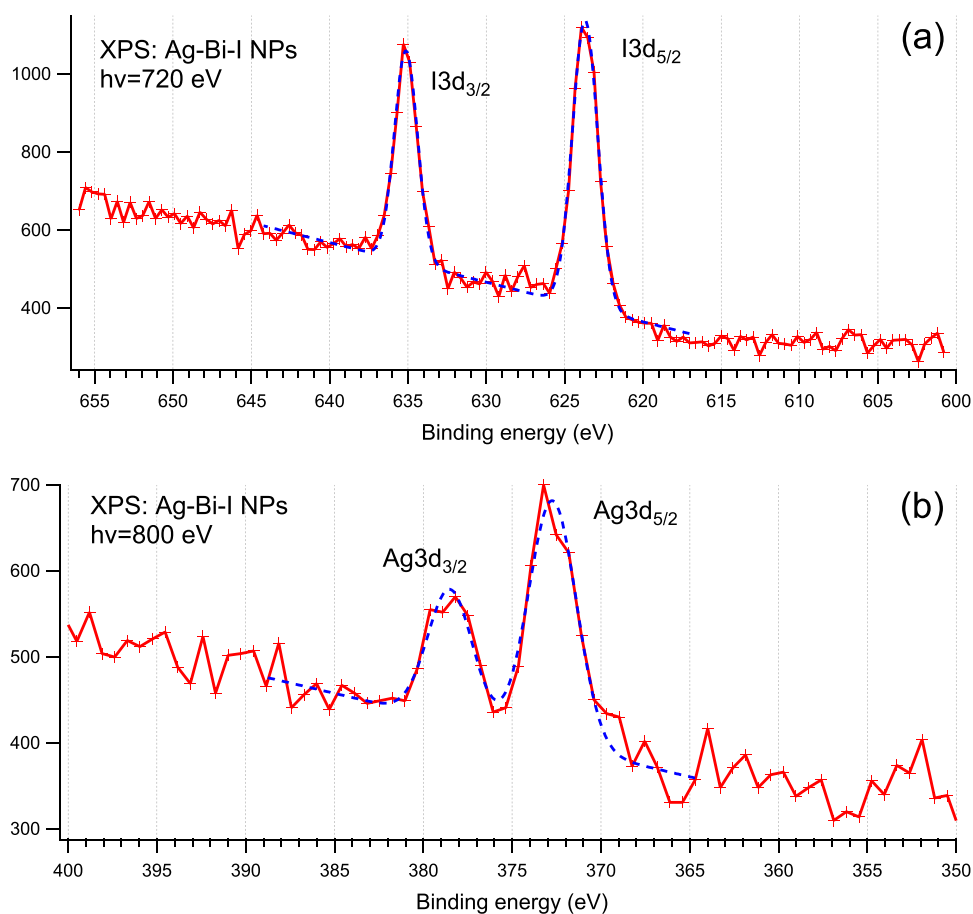


**Figure 2.** Gas-phase XPS of isolated  $\text{Ag}_3\text{Bi}$  nanoparticles recorded around I and Ag 3d edges, at photon energies of 720 and 800 eV, respectively. Blue dotted lines represent a 2-peak fit to the experimental points.

permanent magnet APPLE II type undulator, with a period of 80 mm, in combination with a high-flux, 600 L/mm grating of the modified Petersen plane grating monochromator used to monochromatize the synchrotron radiation. For the used photon energies of 100, 380, 720, and 800 eV, the exit slit was set to 300, 200, 250, and 550  $\mu\text{m}$ , respectively, which in combination with an appropriate Scienta analyzer slit size and its pass energy (100 or 200 eV in the present case) yielded an overall resolution in the XPS spectra of about 0.1, 0.5, 1.5, and 3.5 eV, respectively. The linearity of the photoelectron kinetic energy scale has been calibrated according to the 3p, 3s, 2p, and 2s Ar IPs,<sup>14,15</sup> as well as Ar  $L_3M_{23}M_{23}$  Auger line,<sup>16</sup> measured by a Scienta XPS spectrometer under the same experimental conditions. The Ar gas was introduced in the ionization chamber using the same MPSC chamber setup, through the ALS and the skimmer. The photon energy calibration was performed according to several different transitions: Ar( $2p_{3/2}^{-1} \rightarrow 4s$ ) at 244.39 eV,<sup>17</sup>  $\text{N}_2(\text{N } 1s, \nu = 0 \rightarrow \pi^*)$  at 400.865,<sup>18</sup> and Ne ( $1s \rightarrow 3p$ ) at 867.14 eV.<sup>19</sup> Calibration gases were introduced into the calibration chamber (downstream to the XPS measurements) by an effusive jet crossing at the right angle of the SR beam. Resulting photoions were extracted and detected by a large-circular opening single-channel multiplier (“Dr. Sjuts Optotechnik GmbH” – model KBL 25RS) connected to pulse counting electronics. The overall accuracy of the photon energy calibration in the whole energy range was estimated to be 0.2 eV, not including the accuracy of the literature values used as reference points.

The binding energy (BE) scale with respect to the vacuum level, of each particular recorded XPS spectrum, was calibrated solely according to an appropriate closely lying XPS line that corresponds to particular ionization energy (IE) of Ar or  $\text{N}_2$  carrier gases. For consistency, considering possible dispersion of the existing reference XPS values, we have decided to calibrate all XPS spectra according to only two IEs: (1) all inner-shell spectra (except for I 4d) were calibrated according to  $\text{N}_2$  N1s IE reported at 409.9 eV;<sup>14</sup> (2) all valence spectra and I 4d were calibrated according to Ar  $3p_{3/2}$  IE at 15.76 eV.<sup>20</sup> Note that an uncertainty in the incident photon energy does not influence the calibration of the binding energy scale, which only depends on the uncertainty in the linearity of the photoelectron kinetic energy scale and the error of the reference IE value. The overall uncertainty of BE due to the calibration is estimated to be 0.1–0.2 eV.

A detailed description of the performed electronic structure calculations of  $\text{BiI}_3$  and Ag-Bi-I materials is provided in the Supporting Information. Since previous studies<sup>2,4</sup> imply that different Ag-Bi-I materials have a rather similar electronic structure, we have used the  $\text{AgBiI}_4$  material as their representative in the calculations. This material has the smallest primitive cell among different Ag-Bi-I materials, and for this reason, the calculation of its electronic structure is possible even with a more computationally demanding approach based on hybrid functionals.

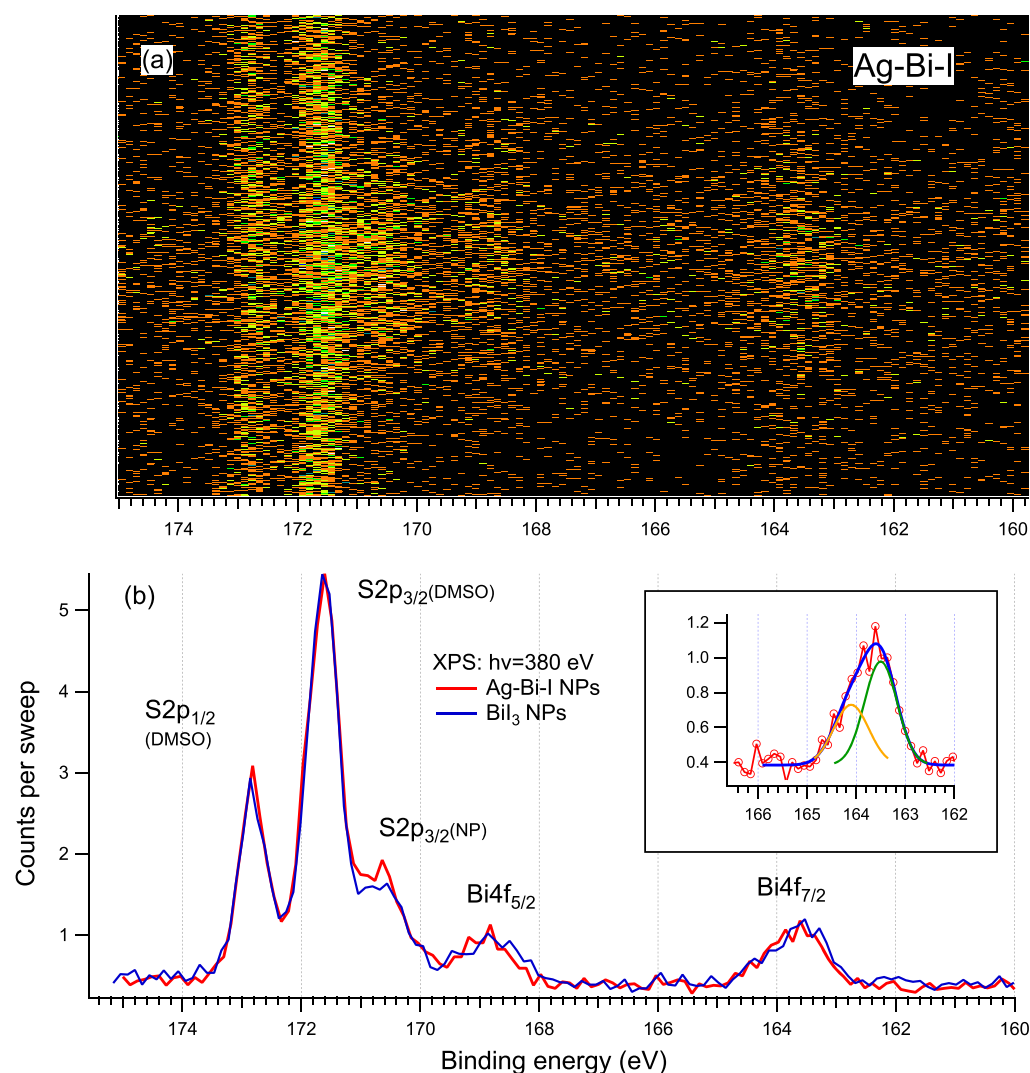


**Figure 3.** Gas-phase XPS photoelectron spectrum in (a) two dimensions and (b) as an integrated spectrum, of isolated  $\text{Ag}_3\text{BiI}_6$  and  $\text{BiI}_3$  nanoparticles recorded around S2p and Bi4f edges, at a photon energy of 380 eV. Vertical axis shows a total number of counts produced in the 162 XPS sweeps of  $\text{Ag}_3\text{BiI}_6$  NPs. Inset in (b) shows two-peak deconvolution of the Bi4f<sub>7/2</sub> peak with maximum positions at: 163.5 and 164.1 eV.

## RESULTS AND DISCUSSION

We consider that the formation of the Ag-Bi-I nanosystems takes place in the gas phase upon the removal of the solvent from the atomized droplets of the AgI/ $\text{BiI}_3$  precursor solution in DMSO (see the Supporting Information for details). The sample collection stages, parallel to the in situ synchrotron radiation XPS of isolated nanosystems, were set for the investigation of the crystal structure, morphology, and chemical composition of the particles formed (Figure S2).

**Characterization of Ag-Bi-I Aerosols.** Figure 1 presents the results of the morphological and chemical characterization of the Ag-Bi-I particles deposited on an appropriate substrate. For structural characterization, the samples were precipitated onto an oriented silicon substrate from the AgI/ $\text{BiI}_3$  DMSO solution at 120 °C. The XRD pattern in Figure 1a exhibits reflections that correspond to the rhombohedral structure of  $\text{Ag}_3\text{BiI}_6$  (R-3 m space group),<sup>21</sup> as well as a small contribution of the AgI phase. A similar XRD pattern of  $\text{Ag}_3\text{BiI}_6$  thin films annealed at 400 K was reported by Turkevych et al.<sup>4</sup> The UV-vis absorption spectra (Figure S3a) of the  $\text{Ag}_3\text{BiI}_6$  particles dispersed in acetonitrile, as well as of the  $\text{Ag}_3\text{BiI}_6$  films deposited on a quartz substrate, showed absorption edges at

~2.2 and ~1.7 eV, respectively, which is in accordance with the previous reports.<sup>4</sup> Figure 1b shows the distribution of mobility diameters of the  $\text{Ag}_3\text{BiI}_6$  and  $\text{BiI}_3$  aerosol particles determined by a scanning mobility particle sizer (E.T.S. and S.I.). The distribution is lognormal and centered at ~80 nm for both samples. The total NP concentration was ~ $10^6$  particles/cm<sup>3</sup>.

For morphological characterization, the aerosol particles were electrostatically precipitated onto an aluminum substrate and investigated by scanning electron microscopy (SEM). Typical SEM images of the  $\text{Ag}_3\text{BiI}_6$  and  $\text{BiI}_3$  aerosols are presented in Figure 1c. Both samples consist of submicrometric, mostly isolated, particles with an average size of ~110 and ~220 nm for the Ag-Bi-I and  $\text{BiI}_3$ , respectively. The details on the distribution of the particle sizes are given in the Supporting Information (Figure S3b). In addition, larger deposits (up to several micrometers in thickness) were sporadically observed due to the aggregation of the particles.  $\text{BiI}_3$  has a two-dimensional layered structure with octahedral  $\text{BiI}_6^{n-}$  units, and its particles indicate a plate-like morphology (Figure 1c); meanwhile, the Ag-Bi-I particles are spherical in shape. As it was discussed by Kim et al.,<sup>6</sup> the transformation of

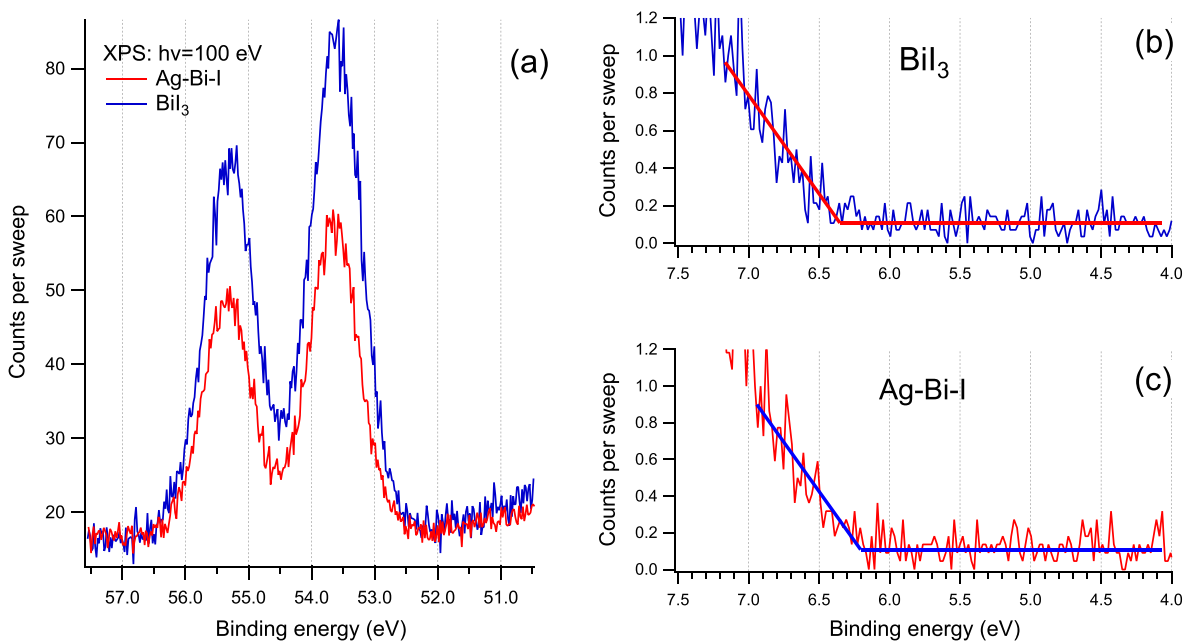


**Figure 4.** Gas-phase XPS of isolated Ag-Bi-I and  $\text{BiI}_3$  nanoparticles around (a) I 4d and (b, c) valence edges, at a photon energy of 100 eV.

the two-dimensional Bi-I structure into a three-dimensional Ag-Bi-I ternary system is a consequence of the incorporation of  $\text{Ag}^+$  ions into the iodobismuthate lattice. In addition, the anisotropy of  $\text{BiI}_3$  particles is probably the reason for the notable difference between the distributions of aerodynamic diameters measured by the SMPS and those observed by SEM (Figure S3b). Figure 1d shows the results of the chemical microanalysis performed on a wide Ag-Bi-I sample area by energy-dispersive X-ray spectroscopy (EDS). It is evident that X-ray signals from the characteristic transitions of silver, bismuth, and iodine originate from the particulate material and colocalize within the image resolution.

**Electronic Structure.** Figure 2 shows XAPS spectra of isolated Ag-Bi-I NPs around iodine and silver 3d edges. The  $\text{I}3\text{d}_{3/2}$  and  $\text{I}3\text{d}_{5/2}$  binding energies (BEs) are determined at 635.1 and 623.7 eV, respectively, while  $\text{Ag}3\text{d}_{3/2}$  and  $\text{Ag}3\text{d}_{5/2}$  BEs are determined at 378.5 and 372.7 eV, respectively. Note that the present gas-phase XPS spectra are referenced to the vacuum level.<sup>8</sup> The BEs of both Ag3d and I3d levels in  $\text{Ag}_3\text{BiI}_6$  are close to that in AgI and  $\text{BiI}_3$ . This is expected, since, in the R-3 m structure of Ag-Bi-I ruderfites, each metal cation is octahedrally coordinated by iodines,<sup>4,21</sup> as in both AgI and  $\text{BiI}_3$ . Indeed, the XPS of thin films also shows practically no shift in the positions of Ag and I3d BEs between  $\text{AgBi}_2\text{I}_7$ ,  $\text{Ag}_2\text{BiI}_5$ , and  $\text{AgBiI}_4$  crystals.<sup>2</sup>

Figure 3 compares XAPS of  $\text{Ag}_3\text{BiI}_6$  and  $\text{BiI}_3$  NPs in the BE regions of S2p and Bi 4f thresholds. A doublet resolved at 172.8 and 171.6 eV clearly corresponds to  $\text{S}2\text{p}_{1/2}$  and  $\text{S}2\text{p}_{3/2}$  of the residual DMSO solvent because the small solvent molecules are not focused by the aerodynamic lens, and the corresponding XPS lines consequently span the entire Y-direction of 2D XPS image as shown in Figure 3a (see Figure S4 and the Supporting Information for details). Note that all inner-shell gas-phase spectra shown here were calibrated using the N1s BE of  $\text{N}_2$  carrier gas to avoid inconsistencies due to reference literature values for different gases (see E.T.S. for more details). Therefore, the DMSO S2p lines appear slightly shifted in comparison to previously published data.<sup>22</sup> On the other hand, two lines at about 168.8 and 163.5 eV clearly come

from the focused NP beam (Figure S4) and correspond to the  $\text{Bi}4\text{f}_{5/2}$  and  $\text{Bi}4\text{f}_{7/2}$ , respectively.

The Bi 4f level does not change significantly after the introduction of silver into the iodobismuthate lattice. The Bi 4f BEs are practically equal in  $\text{Ag}_3\text{BiI}_6$  and  $\text{BiI}_3$  NPs, within the present experimental uncertainty. This was also reported previously for Ag-Bi-I thin films.<sup>2</sup> However, contrary to the later results,<sup>2</sup> the observed Bi 4f peaks do not exhibit lower BE components separated by about 2 eV, corresponding to the metallic bismuth phase ( $\text{Bi}^0$ ), confirming (within the limits of the statistical uncertainty) that produced NPs do not contain the metallic phase.

On the other hand, the Bi  $4\text{f}_{7/2}$  peak shows an asymmetry toward higher BE values. Although the present statistics and spectral resolution do not allow for a definite conclusion, a two-peak deconvolution of this feature suggests an additional feature shifted toward higher BEs for about 0.6 eV (inset in Figure 3b). This feature can be attributed to the presence of a  $\text{Bi}^{2+}$  oxidative state in the system. Furthermore, in addition to the doublet attributed to the sulfinyl groups of the gas-phase DMSO solvent, an additional peak can be distinguished in the S2p spectral region at about 170.6 eV (Figure 3b). According to the 2D XPS image shown in Figure 3, this peak clearly arises from the NP beam (also see Figure S4). The spectral features shown in Figure 3b at  $\sim 164.1$  and  $\sim 170.6$  eV therefore originate from nanophase and can be tentatively assigned to Bi–O–S= moieties. Iversen and co-workers reported that dissolving  $\text{BiI}_3$  in DMSO resulted in the formation of  $\text{Bi}_2\text{I}_9\text{Bi}(\text{C}_2\text{H}_6\text{OS})_8$  molecules,<sup>23</sup> which might also occur in the present case, as suggested by the above XPS assignment. In the abovementioned study,<sup>23</sup>  $\text{Bi}_2\text{I}_9\text{Bi}(\text{C}_2\text{H}_6\text{OS})_8$  was found to be unstable, that is, the casting of the solution resulted in the formation of pure  $\text{BiI}_3$  films. Although XAPS indicates that both Ag-Bi-I and Bi–O–S= species are present in the aerosol beam, the NPs deposited on a substrate did not contain sulfur or oxygen (Figure 1). Consequently, we assert that the observed signal arises due to the presence of the particulate Bi–O–S= species in the aerosol beam, rather than as ligands bound to the Ag-Bi-I NP surface (though the XAPS cannot

determine this unambiguously). Note that the formation of Bi-solvent complexes can also explain the excess of silver atoms in the resulting  $\text{Ag}_3\text{BiI}_6$  NPs, whereas the initial Ag:Bi molar ratio was 2.

The work function (WF) of the gas phase synthesized  $\text{Ag}_3\text{BiI}_6$  NPs was estimated from the difference between the present BEs calibrated to the vacuum level and the existing surface XPS of Ag-Bi-I thin films calibrated to the Fermi level.<sup>2</sup> The surface XPS gives BEs for  $13d_{5/2}$ ,  $\text{Ag}3d_{5/2}$ , and  $\text{Bi}4f_{7/2}$  at 619.3, 368.2, and 158.9 eV, respectively.<sup>2</sup> Therefore, by comparing these results with the present corresponding values of 623.7, 372.7, and 163.5 eV, respectively, one obtains an average WF of 4.5 eV. We note that the WF of isolated ruddorffite NP may be different than the WFs of Ag-Bi-I thin films or the same nanoparticles deposited on a substrate. However, for the size of the particles observed in this study, we do not expect significant differences.<sup>8</sup> In addition, depending on the preparation procedure, the WF can be underestimated due to the presence of the impurities in the nanoparticle beam.

Figure 4a–c shows the I4d inner-shell and valence region spectra for  $\text{Ag}_3\text{BiI}_6$  and  $\text{BiI}_3$  NPs. The spectra were calibrated to the BE of  $\text{Ar}3p_{3/2}$  of the carrier gas (see E.T.S.). Both types of NPs exhibit thresholds at around 6 eV. The minor difference between the ionization energies (IEs) of  $\text{Ag}_3\text{BiI}_6$  and  $\text{BiI}_3$  aligns with the values reported in the literature.<sup>24</sup> The obtained IE of  $6.1 \pm 0.2$  eV for  $\text{Ag}_3\text{BiI}_6$  appears to be slightly lower than that of  $\text{BiI}_3$ , although the experimental uncertainty prevents a more accurate comparison. For this reason, the experimental values of the IEs are also compared to the valence band maxima (VBM) obtained from the electronic structure calculations.

We performed calculations for the bulk Ag-Bi-I and  $\text{BiI}_3$  materials and slabs of these materials that model their interfaces with vacuum. Electronic structures were modeled using density functional theory (DFT) in which the exchange-correlation functional was modeled using either Perdew–Burke–Ernzerhof (PBE) generalized gradient approximation (GGA)<sup>25</sup> or the hybrid PBE0<sup>26,27</sup> functional. The PBE0 functional is known to provide significantly better VBM positions than the PBE functional for a variety of semiconducting materials.<sup>28,29</sup> To obtain the positions of band energies with respect to vacuum, we determine the energy shift necessary for aligning the bulk potential profile with a potential profile in the material slab. We then use this information to determine the positions of bulk band energies with respect to vacuum. We found that when the PBE functional is used, VBM for Ag-Bi-I and  $\text{BiI}_3$  are  $-5.4$  and  $-5.9$  eV, respectively; meanwhile, lower values of  $-6.3$  and  $-6.6$  eV were obtained when using the PBE0 functional. The results obtained from the hybrid PBE0 functional are therefore in agreement with the present experimental results. Moreover, the calculations confirm that the Ag-Bi-I NPs possess slightly lower IE than the  $\text{BiI}_3$  NPs. Additional calculation details are provided in the Supporting Information.

## CONCLUSIONS

To conclude, in this proof of concept study, airborne ligand-free  $\text{Ag}_3\text{BiI}_6$  NPs were successfully fabricated by the atomization of the AgI/ $\text{BiI}_3$  precursors in the DMSO solution. The XAPS showed clear signals from all expected elements Ag, Bi, and I and allowed the estimation of WF of the NPs to be  $4.5 \pm 0.2$  eV. The IE of  $\text{Ag}_3\text{BiI}_6$  NPs was experimentally determined

to be  $6.1 \pm 0.2$  eV, which is in good agreement with the calculation based on a hybrid functional approach.

The novel procedure for the fabrication of ligand-free  $\text{Ag}_3\text{BiI}_6$  particles presented in this work could undergo further optimization and inspire future relevant studies on the aerosol processing of Ag-Bi-I nanomaterials. For example, NPs of different compositions and/or crystal structures could be obtained by changing the concentration of the salts in the precursor solution and/or the temperature in the solvent extraction tube. In addition, the size distribution of the resulting aerosol would depend significantly on the type of atomizer used, since the diameter of the primary droplets produced by the atomizer depends on its construction and operational parameters. Finally, the fabrication process of Ag-Bi-I NPs directly from the precursor solution at low temperatures can be modified by introducing specific molecules into the solution that would act as ligands or spacers. The simple and low-cost fabrication method of Ag-Bi-I nanometer-sized objects presented here could facilitate the scalability and integration of the Ag-Bi-I in the photovoltaic device, thus leading to an enhancement in their performance.

## ASSOCIATED CONTENT

### Supporting Information

The Supporting Information is available free of charge at <https://pubs.acs.org/doi/10.1021/acs.jpcc.0c06819>.

Description of the Ag-Bi-I precursor solution preparation, aerosol generation, and X-ray aerosol photoelectron spectroscopy (XAPS); additional data on the characterization of  $\text{Ag}_3\text{BiI}_6$  nanoparticles and the XPS 2D imaging of small molecules and nanoparticles; and a detailed description of the theoretical methods used (PDF)

## AUTHOR INFORMATION

### Corresponding Authors

**Dušan K. Božanić** – Department of Radiation Chemistry and Physics, "Vinča" Institute of Nuclear Sciences - National Institute of the Republic of Serbia, University of Belgrade, Belgrade 11001, Serbia; [orcid.org/0000-0001-8246-9635](https://orcid.org/0000-0001-8246-9635); Email: [bozanic@vin.bg.ac.rs](mailto:bozanic@vin.bg.ac.rs)

**Aleksandar R. Milosavljević** – SOLEIL, Gif sur Yvette Cedex 91192, France; [orcid.org/0000-0003-3541-8872](https://orcid.org/0000-0003-3541-8872); Email: [milosavljevic@synchrotron-soleil.fr](mailto:milosavljevic@synchrotron-soleil.fr)

### Authors

**Danijela Danilović** – Department of Radiation Chemistry and Physics, "Vinča" Institute of Nuclear Sciences - National Institute of the Republic of Serbia, University of Belgrade, Belgrade 11001, Serbia

**Radovan Dojčilović** – Department of Radiation Chemistry and Physics, "Vinča" Institute of Nuclear Sciences - National Institute of the Republic of Serbia, University of Belgrade, Belgrade 11001, Serbia

**Nenad Vukmirović** – Institute of Physics Belgrade, University of Belgrade, Belgrade 11080, Serbia; [orcid.org/0000-0002-4101-1713](https://orcid.org/0000-0002-4101-1713)

**Pitambar Sapkota** – Radiation Laboratory and Department of Physics, University of Notre Dame, Notre Dame, Indiana 46556, United States

**Ivana Vukašinović** – Faculty of Agriculture, University of Belgrade, Belgrade 11080, Serbia

Vladimir Djoković – Department of Radiation Chemistry and Physics, "Vinča" Institute of Nuclear Sciences - National Institute of the Republic of Serbia, University of Belgrade, Belgrade 11001, Serbia

John Bozek – SOLEIL, Gif sur Yvette Cedex 91192, France  
Christophe Nicolas – SOLEIL, Gif sur Yvette Cedex 91192, France

Sylwia Ptasińska – Radiation Laboratory and Department of Physics, University of Notre Dame, Notre Dame, Indiana 46556, United States; [orcid.org/0000-0002-7550-8189](https://orcid.org/0000-0002-7550-8189)

Complete contact information is available at:  
<https://pubs.acs.org/10.1021/acs.jpcc.0c06819>

## Notes

The authors declare no competing financial interest.

## ACKNOWLEDGMENTS

P.S. and S.P. acknowledge the U.S. Department of Energy Office of Science, Office of Basic Energy Sciences, under Award Number DE-FC02-04ER15533 (NDRL# 5292). D.D., D.K.B., R.D., V.D.J., I.V., and N.V. acknowledge the support from the Ministry of Education, Science and Technological Development of the Republic of Serbia. Numerical simulations were run on the PARADOX-IV supercomputing facility at the Scientific Computing Laboratory, National Center of Excellence for the Study of Complex Systems, Institute of Physics Belgrade. SOLEIL's support is acknowledged under project no. 20190421. The authors also thank the technical staff of SOLEIL for the smooth and efficient running of the facility, as well as Dr. Laurent Nahon for useful discussions and support.

## REFERENCES

- (1) Sansom, H. C.; Whitehead, G. F. S.; Dyer, M. S.; Zanella, M.; Manning, T. D.; Pitcher, M. J.; Whittles, T. J.; Dhanak, V. R.; Alaria, J.; Claridge, J. B.; et al. AgBiI<sub>4</sub> as a Lead-Free Solar Absorber with Potential Application in Photovoltaics. *Chem. Mater.* **2017**, *29*, 1538–1549.
- (2) Khazaei, M.; Sardashti, K.; Chung, C. C.; Sun, J. P.; Zhou, H.; Bergmann, E.; Dunlap-Shohl, W. A.; Han, Q.; Hill, I. G.; Jones, J. L.; et al. Dual-Source Evaporation of Silver Bismuth Iodide Films for Planar Junction Solar Cells. *J. Mater. Chem. A* **2019**, *7*, 2095–2105.
- (3) Jung, K. W.; Sohn, M. R.; Lee, H. M.; Yang, I. S.; Sung, S. D.; Kim, J.; Wei-Guang Diao, E.; Lee, W. I. Silver Bismuth Iodides in Various Compositions as Potential Pb-Free Light Absorbers for Hybrid Solar Cells. *Sustain. Energy Fuels* **2018**, *2*, 294–302.
- (4) Turkevych, I.; Kazaoui, S.; Ito, E.; Urano, T.; Yamada, K.; Tomiyasu, H.; Yamagishi, H.; Kondo, M.; Aramaki, S. Photovoltaic Rudorffites: Lead-Free Silver Bismuth Halides Alternative to Hybrid Lead Halide Perovskites. *ChemSusChem* **2017**, *10*, 3754–3759.
- (5) Zhu, H.; Pan, M.; Johansson, M. B.; Johansson, E. M. J. High Photon-to-Current Conversion in Solar Cells Based on Light-Absorbing Silver Bismuth Iodide. *ChemSusChem* **2017**, *10*, 2592–2596.
- (6) Kim, Y.; Yang, Z.; Jain, A.; Voznyy, O.; Kim, G.-H.; Liu, M.; Quan, L. N.; de Arquer, F. P. G.; Comin, R.; Fan, J. Z.; et al. Pure Cubic-Phase Hybrid Iodobismuthates AgBi<sub>2</sub>I<sub>7</sub> for Thin-Film Photovoltaics. *Angew. Chem., Int. Ed.* **2016**, *55*, 9586–9590.
- (7) Sublemontier, O.; Nicolas, C.; Aureau, D.; Patanen, M.; Kintz, H.; Liu, X.; Gaveau, M. A.; Le Garrec, J. L.; Robert, E.; Barreda, F. A.; et al. X-Ray Photoelectron Spectroscopy of Isolated Nanoparticles. *J. Phys. Chem. Lett.* **2014**, *5*, 3399–3403.
- (8) Milosavljević, A. R.; Božanić, D. K.; Sadhu, S.; Vukmirović, N.; Dojčilović, R.; Sapkota, P.; Huang, W.; Bozek, J.; Nicolas, C.; Nahon, L.; et al. Electronic Properties of Free-Standing Surfactant-Capped

Lead Halide Perovskite Nanocrystals Isolated in Vacuo. *J. Phys. Chem. Lett.* **2018**, *9*, 3604–3611.

(9) Klein-Kedem, N.; Cahen, D.; Hodes, G. Effects of Light and Electron Beam Irradiation on Halide Perovskites and Their Solar Cells. *Acc. Chem. Res.* **2016**, *49*, 347–354.

(10) Barrows, A. T.; Pearson, A. J.; Kwak, C. K.; Dunbar, A. D. F.; Buckley, A. R.; Lidzey, D. G. Efficient Planar Heterojunction Mixed-Halide Perovskite Solar Cells Deposited via Spray-Deposition. *Energy Environ. Sci.* **2014**, *7*, 2944–2950.

(11) Bishop, J. E.; Routledge, T. J.; Lidzey, D. G. Advances in Spray-Cast Perovskite Solar Cells. *J. Phys. Chem. Lett.* **2018**, *9*, 1977–1984.

(12) Bag, S.; Deneault, J. R.; Durstock, M. F. Aerosol-Jet-Assisted Thin-Film Growth of CH<sub>3</sub>NH<sub>3</sub>PbI<sub>3</sub> Perovskites—A Means to Achieve High Quality, Defect-Free Films for Efficient Solar Cells. *Adv. Energy Mater.* **2017**, *7*, 1–11.

(13) Lindblad, A.; Söderström, J.; Nicolas, C.; Robert, E.; Miron, C. A Multi Purpose Source Chamber at the PLEIADES Beamline at SOLEIL for Spectroscopic Studies of Isolated Species: Cold Molecules, Clusters, and Nanoparticles. *Rev. Sci. Instrum.* **2013**, *84*, 113105.

(14) Svensson, S.; Eriksson, B.; Mårtensson, N.; Wendin, G.; Gelius, U. Electron Shake-up and Correlation Satellites and Continuum Shake-off Distributions in x-Ray Photoelectron Spectra of the Rare Gas Atoms. *J. Electron. Spectros. Relat. Phenomena.* **1988**, *47*, 327–384.

(15) Thompson, A.; Attwood, D.; Gullikson, E.; Howells, M.; Kim, K.-J.; Kirz, J.; Kortright, J.; Lindau, I.; Liu, Y.; Pianetta, P.; et al. *X-Ray Data Booklet*; Lawrence Berkeley National Laboratory, 2009.

(16) Werme, L. O.; Bergmark, T.; Siegbahn, K. The L<sub>2,3</sub> MM Auger Spectrum of Argon. *Phys. Scr.* **1973**, *8*, 149–153.

(17) Nicolas, C.; Miron, C. Lifetime Broadening of Core-Excited and -Ionized States. *J. Electron Spectros. Relat. Phenomena* **2012**, *185*, 267–272.

(18) Kato, M.; Morishita, Y.; Oura, M.; Yamaoka, H.; Tamenori, Y.; Okada, K.; Matsudo, T.; Gejo, T.; Suzuki, I. H.; Saito, N. Absolute Photoionization Cross Sections with Ultra-High Energy Resolution for Ar, Kr, Xe and N<sub>2</sub> in Inner-Shell Ionization Regions. *J. Electron. Spectros. Relat. Phenomena.* **2007**, *160*, 39–48.

(19) Coreno, M.; Avaldi, L.; Camilloni, R.; Prince, K. C.; de Simone, M.; Karvonen, J.; Colle, R.; Simonucci, S. Measurement and Ab Initio Calculation of the Ne Photoabsorption Spectrum in the Region of the K Edge. *Phys. Rev. A* **1999**, *59*, 2494–2497.

(20) Božanić, D. K.; Garcia, G. A.; Nahon, L.; Sredojević, D.; Lazić, V.; Vukoje, I.; Ahrenkiel, S. P.; Djoković, V.; Šljivančanin, Ž.; Nedeljković, J. M. Interfacial Charge Transfer Transitions in Colloidal TiO<sub>2</sub> Nanoparticles Functionalized with Salicylic Acid and 5-Aminosalicylic Acid: A Comparative Photoelectron Spectroscopy and DFT Study. *J. Phys. Chem. C* **2019**, *123*, 29057–29066.

(21) Oldag, T.; Aussieker, T.; Keller, H.-L.; Preitschaft, C.; Pfitzner, A. Solvothermal Synthesis and Crystal Structure Determination of AgBiI<sub>4</sub> and Ag<sub>3</sub>BiI<sub>6</sub>. *Z. Anorg. Allg. Chem.* **2005**, *36*, 677–682.

(22) Sze, K. H.; Brion, C. E.; Tronc, M.; Bodeur, S.; Hitchcock, A. P. Inner and Valence Shell Electronic Excitation of Dimethyl Sulfoxide by Electron Energy Loss and Photoabsorption Spectroscopies. *Chem. Phys.* **1988**, *121*, 279–297.

(23) Nørby, P.; Vogel Jørgensen, M. R.; Johnsen, S.; Brummerstedt Iversen, B. Bismuth Iodide Hybrid Organic-Inorganic Crystal Structures and Utilization in Formation of Textured BiI<sub>3</sub> Film. *Eur. J. Inorg. Chem.* **2016**, *2016*, 1389–1394.

(24) Crovetto, A.; Hajjifarassar, A.; Hansen, O.; Seger, B.; Chorkendorff, I.; Vesborg, P. C. K. Parallel Evaluation of the BiI, BiOI, and Ag BiI Layered Photoabsorbers. *Chem. Mater.* **2020**, *32*, 3385.

(25) Perdew, J. P.; Burke, K.; Ernzerhof, M. Generalized Gradient Approximation Made Simple. *Phys. Rev. Lett.* **1996**, *77*, 3865–3868.

(26) Perdew, J. P.; Ernzerhof, M.; Burke, K. Rationale for Mixing Exact Exchange with Density Functional Approximations Rationale for Mixing Exact Exchange with Density Functional Approximations. *J. Chem. Phys.* **1996**, *105*, 9982–9985.

(27) Adamo, C.; Barone, V. Toward Reliable Density Functional Methods without Adjustable Parameters: The PBE0 Model. *J. Chem. Phys.* **1999**, *110*, 6158–6170.

(28) Chen, W.; Pasquarello, A. Band-Edge Levels in Semiconductors and Insulators: Hybrid Density Functional Theory versus Many-Body Perturbation Theory. *Phys. Rev. B* **2012**, *86*, 035134.

(29) Steiner, K.; Chen, W.; Pasquarello, A. Band Offsets of Lattice-Matched Semiconductor Heterojunctions through Hybrid Functionals and  $G_0 W_0$ . *Phys. Rev. B* **2014**, *89*, 205309.

## Supporting Information

# Aerosol Synthesis and Gas-Phase Photoelectron Spectroscopy of Ag-Bi-I Nanosystems

*Danijela Danilović<sup>[1]</sup>, Dušan K. Božanić<sup>[1],\*</sup>, Radovan Dojčilović<sup>[1]</sup>, Nenad Vukmirović<sup>[2]</sup>, Pitambar Sapkota<sup>[3,4]</sup>, Ivana Vukašinić<sup>[5]</sup>, Vladimir Djoković<sup>[1]</sup>, John Bozek<sup>[6]</sup>, Christophe Nicolas<sup>[6]</sup>, Sylwia Ptasinska<sup>[3,4]</sup>, and Aleksandar R. Milosavljević<sup>[6],\*</sup>*

<sup>1</sup>*Department of Radiation Chemistry and Physics, "Vinča" Institute of Nuclear Sciences - National Institute of the Republic of Serbia, University of Belgrade, P.O. Box 522, 11001 Belgrade, Serbia*

<sup>2</sup>*Institute of Physics Belgrade, University of Belgrade, Pregrevica 118, 11080, Belgrade, Serbia*

<sup>3</sup>*Radiation Laboratory, University of Notre Dame, Notre Dame, IN 46556, USA*

<sup>4</sup>*Department of Physics, University of Notre Dame, Notre Dame, IN 46556, USA*

<sup>5</sup>*Faculty of Agriculture, University of Belgrade, Nemanjina 6, 11080 Belgrade, Serbia*

<sup>6</sup>*SOLEIL, l'Orme des Merisiers, St. Aubin, BP48, 91192 Gif sur Yvette Cedex, France*

*Corresponding Authors: \*D.K.B. [bozanic@vin.bg.ac.rs](mailto:bozanic@vin.bg.ac.rs); \*A.R.M. [milosavljevic@synchrotron-soleil.fr](mailto:milosavljevic@synchrotron-soleil.fr)*

## EXPERIMENTAL SECTION

### *Ag-Bi-I precursor solution*

The Ag-Bi-I precursor solution in dimethyl sulfoxide (DMSO) was prepared by homogenization of 234 mg of AgI and 295 mg of BiI<sub>3</sub> in mortar and subsequent dispersion of the homogenized powder in 50 ml of DMSO. The resulting of 1.058 wt./vol.% precursor solution was clear and without precipitate, as it is shown in Figure S1.

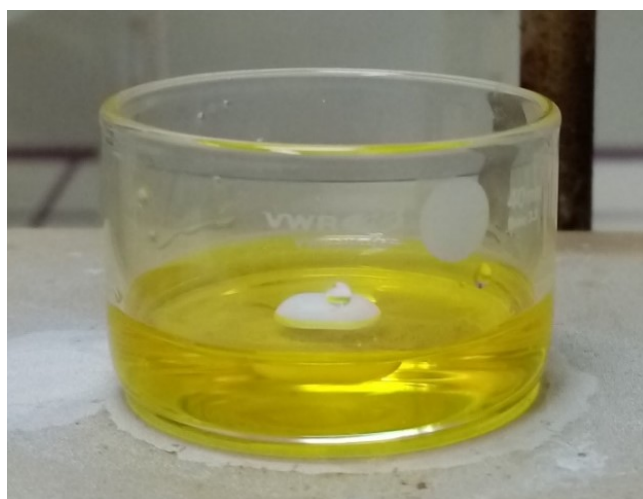


**Figure S1.** Photograph of 1.058 wt./vol.% AgI/BiI<sub>3</sub> precursor solution in DMSO.

### *Aerosol generation and X-ray aerosol photoelectron spectroscopy (XAPS)*

The system for Ag-Bi-I aerosols generation and X-ray aerosol photoelectron spectroscopy (XAPS) is schematically presented in Figure S2. The aerosols were generated by atomization of the precursor solution using TSI 3076 atomizer, then transported using 2.5 bar of either Ar or N<sub>2</sub> carrier gas (depending on the desired photoelectron kinetic energy range) first through a metallic tube (heated to a temperature of about 120 °C to evaporate DMSO), and then through a cold trap (cooled to 0 °C to remove excess DMSO from the beam).

XAPS was performed at the PLEIADES beamline at SOLEIL synchrotron, France, using the Multi-Purpose Source Chamber (MPSC) setup described in details previously.<sup>1</sup> After the generation of Ag-Bi-I nanoparticle (NP) aerosols and removal of excess DMSO solvent (see above), the aerosols were introduced in the MPSC differentially pumped chamber through a 200 μm limiting orifice, followed by an aerodynamic lens system (ALS) that focuses the NP beam through a skimmer to the ionization chamber at 10<sup>-8</sup> mbar base pressure (10<sup>-6</sup>-10<sup>-5</sup> mbar working pressure). The Ag-Bi-I NP beam was crossed by a vertically linearly

polarized synchrotron radiation photon beam in front of an electron energy analyzer. Both the exit of ALS and the skimmer position can be remotely controlled to align the nanoparticle beam to both the photon beam and the focal point of the electron analyzer. The aerosol source conditions were stable during the experiment and XPS spectra did not show any systematic change over the time related to its parameters.

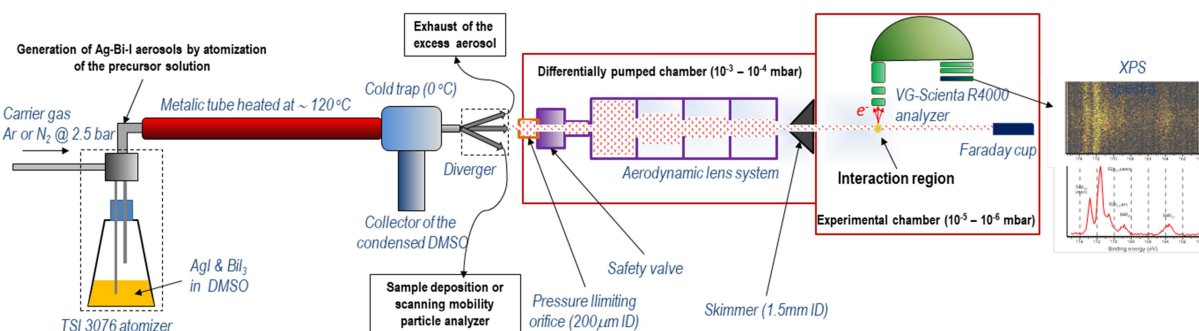


**Figure S2.** Schematic representation of the setup used for Ag-Bi-I aerosol generation and X-ray aerosol photoelectron spectroscopy (XAPS) at the PLEIADES beamline at SOLEIL synchrotron (France).

### *Additional data on the characterization of $\text{Ag}_3\text{BiI}_6$ nanoparticles*

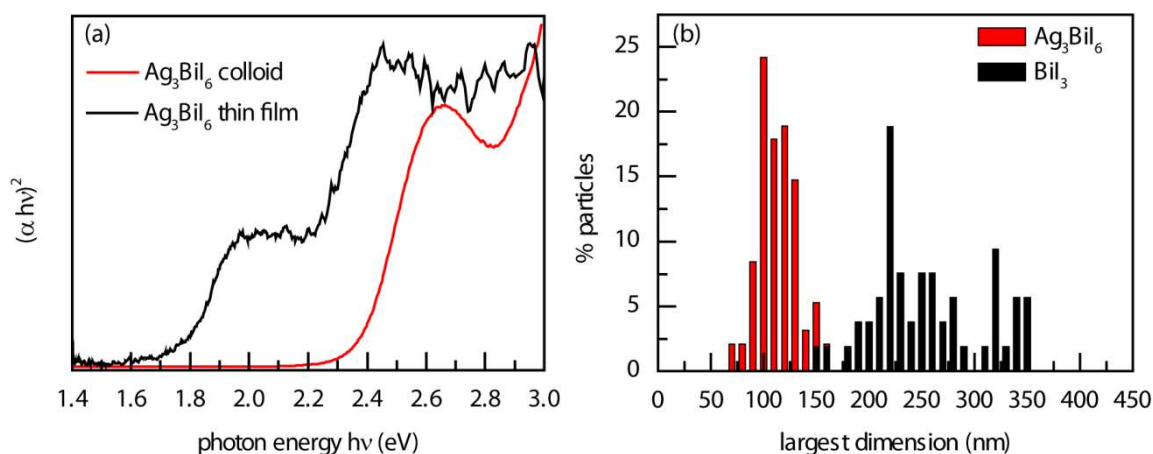


**Figure S3.** (a) Optical absorption spectra of  $\text{Ag}_3\text{BiI}_6$  particles dispersed in acetonitrile (red line) and of a thin  $\text{Ag}_3\text{BiI}_6$  film deposited on a quartz substrate (black line). (b) Distribution of the largest dimensions of the  $\text{Ag}_3\text{BiI}_6$  and  $\text{BiI}_3$  particles observed by SEM (Figures 1c and 1d).

### *XPS of nanoparticles and gas phase molecules*

The aerodynamic lens system (see Figure S2) focuses the nanoparticle (NP) beam and thus provides a high NP target density in the interaction region, leading to a sufficiently high

photoelectron signal to noise ratio, which is necessary to perform XPS spectroscopy of desired target species. Moreover, the focused NP beam also allows to distinguish an XPS signal related to the photoionization of NPs from the one originating from small atoms/molecules such as carrier gas, residual solvent and air background.

Figure S4 schematically represents principles of the XPS spectroscopy of a NP beam using the VG-Scienta R4000 electron energy analyzer at PLEIADES beamline. After being focused by the aerodynamic lens, the NP beam enters the ionization chamber through a skimmer and crosses perpendicularly the photon beam in front of the Scienta analyzer entrance lens (not shown in the scheme). The aerodynamic lens is designed to focus large nanoparticles (50-500 nm), whereas small species such as carrier gas (Ar, N<sub>2</sub>, air) or residual solvent molecules (H<sub>2</sub>O, ethanol, ACN, DMSO etc.) diffuse at the exit of the lens. Therefore, majority of these molecules do not pass through the skimmer and stay in the differentially pumped MPSC chamber, resulting in a low working pressure in the ionization chamber (Figure S2). Part of the carrier gas and residual solvent still makes through the skimmer but since not focused quickly fill a large volume of the ionization chamber (Figure S4, left).

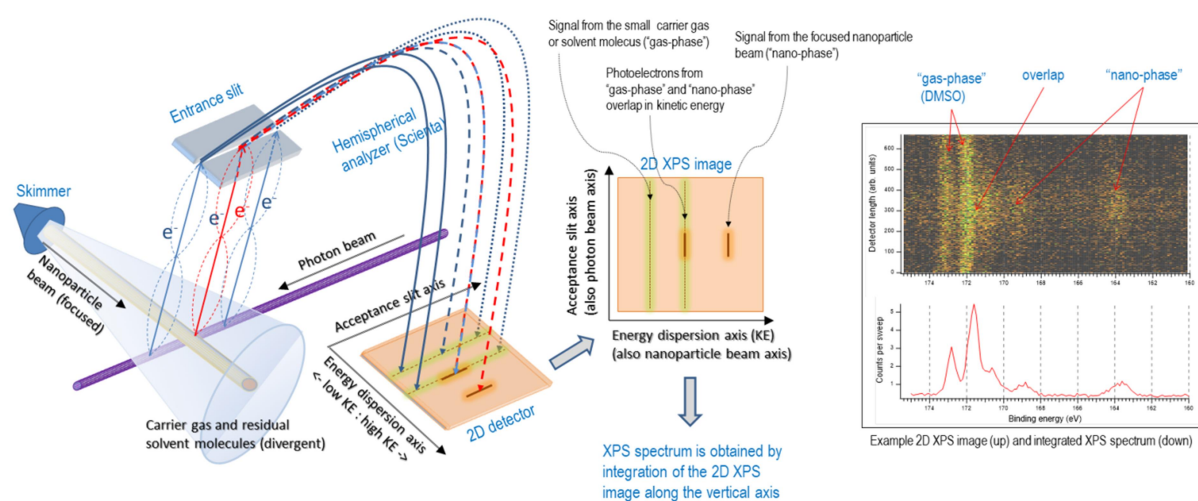


**Figure S4.** Schematic representation of the 2D XPS imaging of a nanoparticle beam at the PLEIADES beamline at SOLEIL synchrotron (France), as well as an example X-ray photoelectron spectrum in two-dimensions (top) and as an integrated spectrum (bottom).

The photon beam ionizes both the focused NP beam and the small molecules along its path and produces photoelectrons. The kinetic energy distribution of the photoelectrons is obtained by dispersing their trajectories inside a hemispherical analyzer, according to their kinetic energies in the horizontal direction onto a position sensitive detector, as schematically

presented in Figure S4. Only photoelectrons produced within a limited interaction area defined roughly by the entrance slit are detected. When Scienta analyzer works in a so called “transmission mode”, all electrons emitted along the axis of the ionizing photon beam are focused to the same vertical position of the detector, independently from their emission angles. Consequently, photoelectrons from the central (along the photon beam direction) part of the interaction region are imaged onto the central (along Y-axis) part of the 2D XPS image (see Figure S4, middle). Note that the axis of the electron energy dispersion (X-axis on the 2D XPS image) coincides with the axis of the nanoparticle beam direction. On the other hand, the axis of the entrance slit (Y-axis of the 2D XPS image) coincidence with the photon beam direction.

Since large NPs are focused to form a beam of sub-millimetre cross-section diameter (typically a few hundred microns), which is markedly smaller than the Scienta entrance slit length, the photoelectrons coming from the NP beam are imaged only onto the central part (along Y-axis) of the 2D XPS image. On the other hand, the photoelectrons coming from the carrier gas and residual solvent molecules fill the whole area of entrance slit because the former are not focused thus form a diffuse cloud around the central nanoparticle beam. Therefore, photoelectron lines corresponding to the nanoparticle beam (“nano-phase”) are seen in the center of the image while those from the gaseous non-focused species (“gas-phase”) fill the whole image, allowing the two components to be easily identified. Note also that the background is dominantly produced from dense nanoparticle beam.

## THEORETICAL SECTION

### *Calculations based on PBE GGA functional within DFT*

Electronic structure calculations based on density functional theory (DFT) were performed. Exchange correlation functional was modelled using Perdew–Burke–Ernzerhof (PBE) generalized gradient approximation (GGA).<sup>2</sup> Effects of spin-orbit interaction were fully included. The effect of core electrons was modeled using norm-conserving fully relativistic pseudopotentials.<sup>3,4</sup>

Calculations were performed using the plane-wave code Quantum Espresso.<sup>5,6</sup> Atomic coordinates and lattice parameters were relaxed until atomic forces were smaller than  $10^{-3}$  Ry/bohr. Kinetic energy cutoff for plane-wave representation of wave functions was 40 Ry for BiI<sub>3</sub> and 50 Ry for Ag-Bi-I. The structures considered and their lattice parameters obtained after relaxation are summarized in Table S1.

**Table S1.** Structures considered and their lattice parameters obtained after relaxation.

- BiI<sub>3</sub>, space group #148  
primitive cell: 2 Bi atoms and 6 I atoms  
unit cell: 6 Bi atoms and 18 atoms  
lattice parameters of hexagonal unit cell:  
 $a = b = 7.25 \text{ \AA}$ ,  $c = 20.58 \text{ \AA}$ ,  $\alpha = \beta = 90^\circ$ ,  $\gamma = 120^\circ$
- AgBiI<sub>4</sub>, space group #74  
primitive cell: 2 Ag, 2 Bi and 8 I atoms  
unit cell: 4 Ag, 4 Bi and 16 I atoms  
lattice parameters of orthorhombic unit cell:  
 $a = 8.35 \text{ \AA}$ ,  $b = 8.26 \text{ \AA}$ ,  $c = 11.93 \text{ \AA}$ ,  $\alpha = \beta = \gamma = 90^\circ$

To obtain the positions of band energies with respect to vacuum, we have performed electronic structure calculation of the system consisting of the interface of the material and the vacuum, see middle parts of Figures S5 and S6. In the case of BiI<sub>3</sub> we considered the system consisting of a BiI<sub>3</sub> slab whose width in  $c$  direction is equal to  $2c$  and a vacuum slab of the same width; see middle part of Fig. S5. In the case of AgBiI<sub>4</sub> we considered the system consisting of a vacuum slab of width  $2c$  and an AgBiI<sub>4</sub> slab whose width in  $c$  direction is equal to  $2c$ , which was terminated with a surface layer containing Ag and I atoms; see middle part of Fig. S6.

The profile of the electronic potential (more precisely the sum of the Hartree potential and the local part of the ionic pseudopotential) in the direction perpendicular to the interface is

presented in the top parts of Figs. S5 and S6. The potential presented in the figures was obtained by averaging in the plane parallel to the interface. The same potential profile for bulk materials is presented in the bottom part of Figs. S5 and S6. To obtain the positions of band energies with respect to vacuum, we determine the energy shift that is necessary to align the bulk potential profile with a potential profile in the material slab. We then use this information to determine the positions of bulk band energies with respect to vacuum.

We find that VBM for  $\text{AgBiI}_4$  and  $\text{BiI}_3$  are respectively -5.4 eV and -5.9 eV when PBE functional is used.

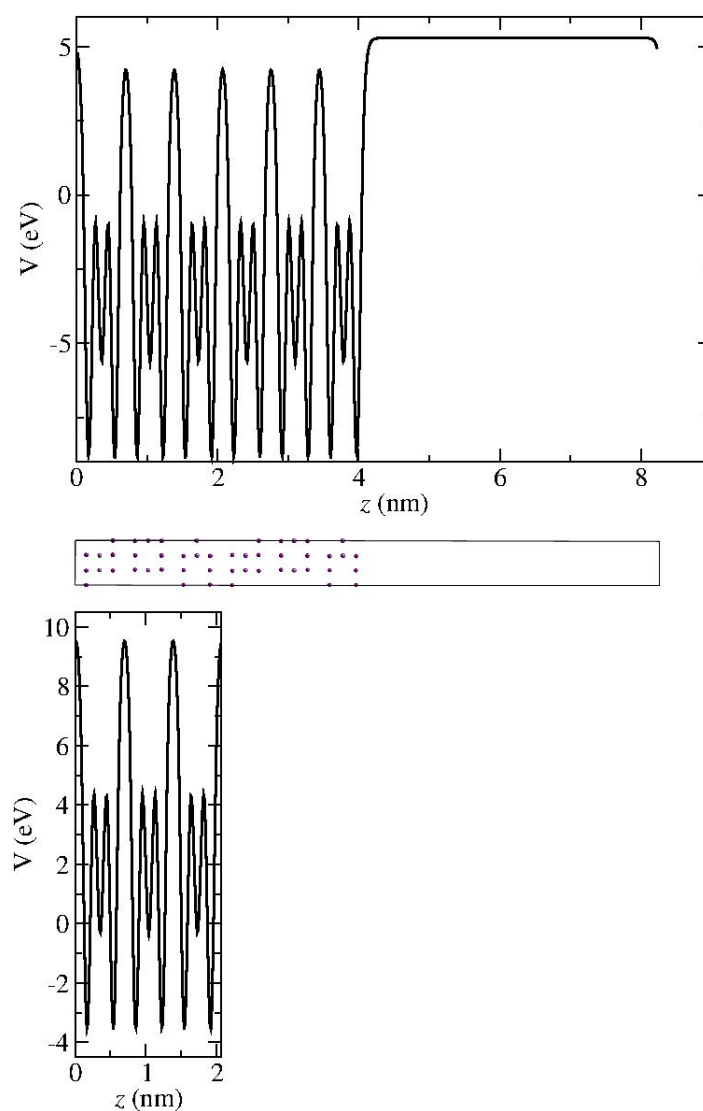


**Figure S5.** Electronic potential profile of the  $\text{BiI}_3$ -vacuum interface (top panel) and bulk  $\text{BiI}_3$  material (bottom panel). Atomic structure of the  $\text{BiI}_3$ -vacuum interface (middle panel).

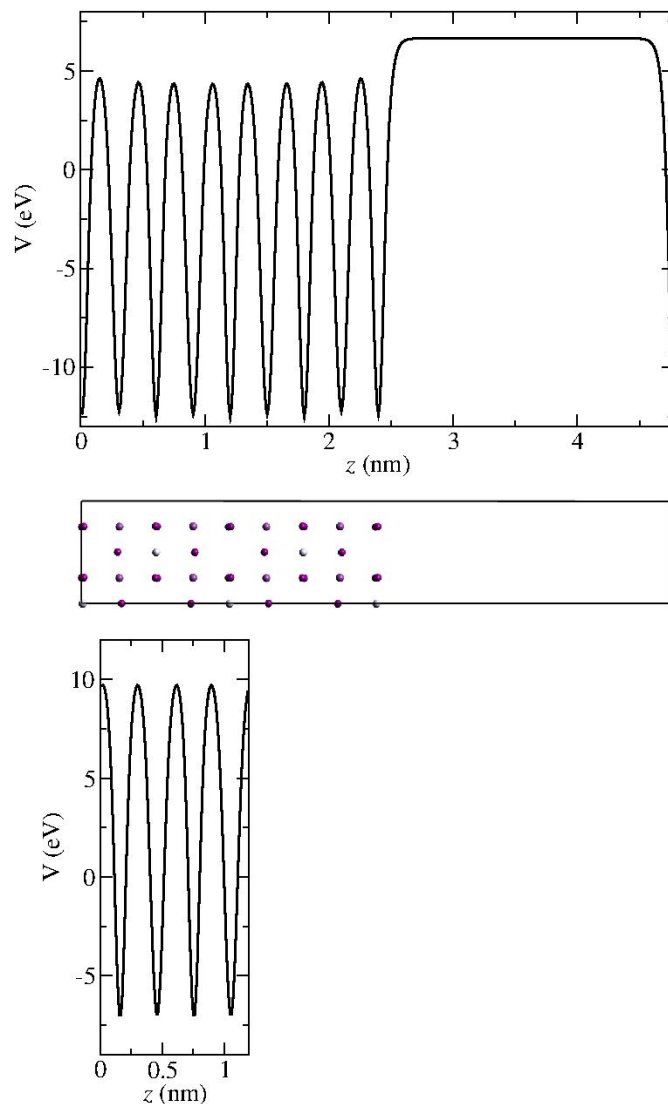


**Figure S6.** Electronic potential profile of the AgBiI<sub>4</sub>-vacuum interface (top panel) and bulk AgBiI<sub>4</sub> material (bottom panel). Atomic structure of the AgBiI<sub>4</sub>-vacuum interface (middle panel).

### *Calculations based on hybrid PBE0 functional*

Electronic structure calculations based on the hybrid PBE0 functional were performed using the same geometry that was used in PBE calculations. The same pseudopotentials and kinetic energy cutoffs as in PBE calculations were used. The PBE0<sup>7,8</sup> functional was used which mixes the Hartree-Fock and PBE exchange energy in 1:3 ratio and takes PBE correlation energy. The PBE0 functional is known to give significantly better energy gaps and VBM positions than the PBE functional for a variety of semiconducting materials (see for example Refs<sup>9,10</sup>). Calculations were performed using the Quantum Espresso code<sup>5,6</sup> which implements the adaptively compressed exchange operator approach for the calculation of exchange energy.<sup>11</sup> 4x4x4 grid of points in reciprocal space was used in the calculation.

To obtain the position of the VBM (and hence the ionization potential) from hybrid functional calculation, we first note that PBE and PBE0 calculations of the same bulk material using the same plane wave computational code have a common energy reference – the average of the electrostatic potential. As a consequence, we obtain the shift of the VBM between PBE and PBE0 calculation simply as the difference of calculated VBMs in the two calculations. We then add this difference to the PBE VBM obtained from the calculation of the interface with vacuum and obtain the PBE0 VBM energy with respect to vacuum. Similar approach for determination of the position of band energies with respect to vacuum was used, for example, in Refs.<sup>9,10,12</sup>

We find that VBM for AgBiI<sub>4</sub> and BiI<sub>3</sub> are respectively -6.3 eV and -6.6 eV when PBE0 functional is used.

We finally discuss the expected differences between the results that would be obtained if Ag<sub>3</sub>BiI<sub>6</sub> instead of AgBiI<sub>4</sub> material were considered in the calculations. Experimental data from Ref.<sup>13</sup> (inset in Fig. 5c therein) suggest that in the sequence AgBi<sub>2</sub>I<sub>7</sub>, AgBiI<sub>4</sub>, Ag<sub>2</sub>BiI<sub>5</sub>, the VBM increases by about 0.1 eV between each two subsequent elements. Extrapolating this trend to Ag<sub>3</sub>BiI<sub>6</sub>, we can estimate that the VBM of Ag<sub>3</sub>BiI<sub>6</sub> would be about 0.2-0.3 eV larger than the VBM of AgBiI<sub>4</sub>. This correction would put the calculated VBM of Ag-Bi-I even closer to our experimental result.

## REFERENCES

- (1) Lindblad, A.; Söderström, J.; Nicolas, C.; Robert, E.; Miron, C. A Multi Purpose Source Chamber at the PLEIADES Beamline at SOLEIL for Spectroscopic Studies of Isolated Species: Cold Molecules, Clusters, and Nanoparticles. *Rev. Sci. Instrum.* **2013**, *84*, 113105. <https://doi.org/10.1063/1.4829718>.
- (2) Perdew, J. P.; Burke, K.; Ernzerhof, M. Generalized Gradient Approximation Made Simple. *Phys. Rev. Lett.* **1996**, *77* (3), 3865–3868.
- (3) Hamann, D. R. Optimized Norm-Conserving Vanderbilt Pseudopotentials. *Phys. Rev. B - Condens. Matter Mater. Phys.* **2018**, *226* (8), 39–54. <https://doi.org/10.1103/PhysRevB.88.085117>.
- (4) van Setten, M. J.; Giantomassi, M.; Bousquet, E.; Verstraete, M. J.; Hamann, D. R.; Gonze, X.; Rignanese, G. M. The PSEUDODOJO: Training and Grading a 85 Element Optimized Norm-Conserving Pseudopotential Table. *Comput. Phys. Commun.* **2018**, *226*, 39–54. <https://doi.org/10.1016/j.cpc.2018.01.012>.
- (5) Giannozzi, P.; Andreussi, O.; Brumme, T.; Bunau, O.; M Buongiorno Nardelli; Calandra, M.; Car, R.; Cavazzoni, C.; Ceresoli, D.; Cococcioni, M.; et al. Advanced Capabilities for Materials Modelling with Quantum ESPRESSO. *J. Phys. Condens. Matter* **2017**, *29*, 465901. <https://doi.org/10.1088/1361-648X/aa8f79>.
- (6) Giannozzi, P.; Baroni, S.; Bonini, N.; Calandra, M.; Car, R.; Cavazzoni, C.; Ceresoli, D.; Chiarotti, G. L.; Cococcioni, M.; Dabo, I.; et al. QUANTUM ESPRESSO: A Modular and Open-Source Software Project for Quantum Simulations of Materials. *J. Phys. Condens. Matter* **2009**, *21* (39), 395502. <https://doi.org/10.1088/0953-8984/21/39/395502>.
- (7) Perdew, J. P.; Ernzerhof, M.; Burke, K. Rationale for Mixing Exact Exchange with Density Functional Approximations. *J. Chem. Phys.* **1996**, *105* (22), 9982–9985. <https://doi.org/10.1063/1.472933>.
- (8) Adamo, C.; Barone, V. Toward Reliable Density Functional Methods without Adjustable Parameters: The PBE0 Model. *J. Chem. Phys.* **1999**, *110* (13), 6158–6170. <https://doi.org/10.1063/1.478522>.
- (9) Chen, W.; Pasquarello, A. Band-Edge Levels in Semiconductors and Insulators: Hybrid Density Functional Theory versus Many-Body Perturbation Theory. *Phys. Rev. B* **2012**, *86*, 035134. <https://doi.org/10.1103/PhysRevB.86.035134>.
- (10) Steiner, K.; Chen, W.; Pasquarello, A. Band Offsets of Lattice-Matched Semiconductor Heterojunctions through Hybrid Functionals and G 0 W 0. *Phys. Rev. B* **2014**, *89*, 205309. <https://doi.org/10.1103/PhysRevB.89.205309>.
- (11) Lin, L. Adaptively Compressed Exchange Operator. *J. Chem. Theory Comput.* **2016**, *12* (5), 2242–2249. <https://doi.org/10.1021/acs.jctc.6b00092>.
- (12) Hinuma, Y.; Kumagai, Y.; Tanaka, I.; Oba, F. Band Alignment of Semiconductors and Insulators Using Dielectric-Dependent Hybrid Functionals : Toward High-Throughput Evaluation. *Phys. Rev. B* **2017**, *95*, 075302. <https://doi.org/10.1103/PhysRevB.95.075302>.
- (13) Khazaee, M.; Sardashti, K.; Chung, C. C.; Sun, J. P.; Zhou, H.; Bergmann, E.; Dunlap-Shohl, W. A.; Han, Q.; Hill, I. G.; Jones, J. L.; et al. Dual-Source Evaporation of Silver Bismuth Iodide Films for Planar Junction Solar Cells. *J. Mater. Chem. A* **2019**, *7* (5), 2095–2105. <https://doi.org/10.1039/c8ta08679f>.